Well-posed spatial marching of perturbations in viscous shear flows

By S. R. Harris AND M. J. P. Hack

1. Motivation and objectives

Although the viscous Navier-Stokes equations are of elliptic type, a parabolic approximation can provide a faithful representation of the full physics at appreciably reduced cost in a range of settings. Within the field of transitional flows, the parabolized stability equations (PSE) have received considerable attention for spatially marching the perturbations. The PSE take advantage of simplifications made possible by the moderate magnitude of non-parallel effects at a sufficient distance from the leading edge. The approximately parabolic nature of the PSE allows their solution through a spatial marching scheme which offers appreciable advantages in terms of computational cost when compared to a classical time-integration approach.

The spatial marching procedure of the PSE nonetheless has several critical limitations. As pointed out by Haj-Hariri (1994), the PSE are not fully parabolic, with the streamwise pressure gradient in the governing equation for the streamwise velocity component introducing residual ellipticity. As discussed by Towne *et al.* (2019), this remaining ellipticity is particularly problematic for upstream-traveling waves which must be damped in some manner to avoid undesired destabilization of the numerical procedure. Established remedies for this problem include the use of an implicit advancement scheme in the streamwise dimension along with a minimum step size (Li & Malik 1996, 1997), the disregard of the streamwise pressure gradient term (Chang *et al.* 1991; Li & Malik 1996), and a modification of the equations which introduces additional damping terms (Andersson *et al.* 1998). As delineated by Towne *et al.* (2019), all these solutions nonetheless have individual disadvantages. While the step size restriction stabilizes the marching procedure, it precludes the convergence of the solution via grid refinement in the streamwise dimension. Depending on the setting, the disregard of the streamwise pressure gradient term can lead to undesirable deviations of the computed results from the physical solution. Similarly, the addition of damping terms can prevent upstream waves from destabilizing the marching procedure, but also dampens the downstream-traveling waves which is undesirable.

For the inviscid case, Towne & Colonius (2015) proposed a solution based on a transformation of the solutions to the Euler equations to characteristic variables and subsequent splitting of physically relevant downstream-traveling waves and computationally problematic upstream-traveling waves. This approach leads to a stable marching procedure at arbitrary grid spacing without modifications to the governing equations. In the presence of viscosity, this approach, however, becomes inaccurate.

Another limitation of the PSE is the capturing of high-amplitude perturbations, as observed during the later stages of the transition process, and in particular also during bypass transition. For natural transition, the PSE have proven valuable in the analysis and modeling of the growth of perturbations in slowly varying shear flows (Herbert 1997; Lozano-Durán *et al.* 2018). However, it was shown by, for instance, Ran *et al.* (2019)

that perturbations with amplitudes beyond 10% of the free-stream convective velocity are inaccurately captured by the PSE, leading, for instance, to erroneous predictions for the growth of secondary instabilities. A closer inspection of the results by Ran *et al.* (2019) demonstrated that the deviation in the mode representing the spanwise invariant distortion to the mean flow, also known as mean-flow distortion (MFD), was the main contributor to the deviation.

In this work, we present a new approach for the spatial marching of disturbances that overcomes these limitations of the classical PSE. In Section 2, we present an approach for the well-posed spatial marching of perturbations in viscous flows that avoids modifications to the governing equations while allowing arbitrarily small streamwise marching steps. In Section 3, we introduce a robust treatment for capturing the MFD based on the spatial marching of both the base state and the perturbations in a nonlinear iterative framework. In section 4, we present our conclusions.

2. Well-posed spatial marching

2.1. *Methodology*

The key element of the spatial marching scheme presented in the following is the decomposition of the local solution at a given streamwise location into upstream- and downstream-traveling waves. For downstream-traveling solutions, which describe, for instance, streamwise amplifying instability waves, the spatial marching approach leads to a well-posed problem. However, upstream-traveling solutions cannot be advanced in this manner, resulting in numerical instabilities which have previously been addressed by either physically unmotivated modifications of the governing equations or reliance on the damping properties of implicit advancement schemes, as discussed above.

In viscous flow, a rigorous indicator for the directionality of a wave-like perturbation is given by its group velocity,

$$c_g = \frac{\partial \omega}{\partial \alpha}, \tag{2.1}$$

where α is the streamwise wavenumber and ω is the angular frequency of the perturbations. If the group velocity is positive, $c_g > 0$, the corresponding eigenfunction describes a downstream-traveling solution. The case $c_g < 0$ identifies upstream-traveling solutions. To evaluate the group velocity, we apply linear stability theory (LST) under the assumption of a wall-parallel base flow, $\boldsymbol{U} = (U(y), 0, 0, 0)^\mathsf{T}$.

The homogeneity of the base state in the time, streamwise, and transverse dimensions enables a normal-mode assumption, and the perturbation velocity and pressure state vector $\boldsymbol{q}' = [u', v', w', P']^\mathsf{T}$ are thus expressed by

$$\boldsymbol{q}'(x, y, z, t) = \hat{\boldsymbol{q}}(y) \exp(i(-\omega t + \alpha x + \beta z)) + c.c., \tag{2.2}$$

where β is the spanwise wavenumber and $\hat{\boldsymbol{q}}(y)$ is the decomposed state vector of the perturbation velocity and pressure. In the following, we consider the spatial stability problem, implying that the frequency, ω, and the spanwise wavenumber, β, are real quantities. Upon substitution into the linearized governing equations, solutions are found only for certain pairs of $\boldsymbol{q}$ and complex streamwise wavenumber α, thus giving rise to an eigenvalue problem. The appearance of α to the second power in the viscous equations further implies that the eigenvalue problem is polynomial in nature. A possible solution technique involves the inflation of the system, as outlined in Appendix A.

Using the definition of the operators given in the Appendix, we can write the eigenvalue problem in the form

$$\mathsf{L}\hat{\boldsymbol{q}} = \alpha \mathsf{M}\hat{\boldsymbol{q}}. \tag{2.3}$$

The evaluation of the group velocity makes use of the adjoint eigenvalue problem,

$$\mathsf{L}^\dagger \hat{\boldsymbol{q}}^\dagger = \alpha^\dagger \mathsf{M}\hat{\boldsymbol{q}}^\dagger, \tag{2.4}$$

where superscript † denotes the adjoint. To each eigensolution of the forward problem, Eq. (2.3), the eigenvalue problem, Eq. (2.4), yields an adjoint eigensolution, with the adjoint eigenvalue being the complex conjugate of the forward eigenvalue, $\alpha^\dagger = \alpha^*$.

Taking the derivative of Eq. (2.3) with respect to ω gives

$$\frac{\partial \mathsf{L}}{\partial \omega}\hat{\boldsymbol{q}} + \mathsf{L}\frac{\partial \hat{\boldsymbol{q}}}{\partial \omega} = \frac{\partial \alpha}{\partial \omega}\mathsf{M}\hat{\boldsymbol{q}} + \alpha\frac{\partial \mathsf{M}}{\partial \omega}\hat{\boldsymbol{q}} + \alpha\mathsf{M}\frac{\partial \hat{\boldsymbol{q}}}{\partial \omega}. \tag{2.5}$$

Knowing the structure of M shows that it is not a function of ω. We define here the inner product such that

$$\langle \boldsymbol{q}_1, \boldsymbol{q}_2 \rangle = \int_0^\infty \boldsymbol{q}_2^{\mathsf{H}} \boldsymbol{q}_1 \mathrm{d}y, \tag{2.6}$$

where superscript H denotes the complex conjugate transpose. Taking the inner product with the associated adjoint eigenfunction, $\boldsymbol{q}^\dagger$, we obtain

$$\langle \frac{\partial \mathsf{L}}{\partial \omega}\hat{\boldsymbol{q}}, \hat{\boldsymbol{q}}^\dagger \rangle + \langle (\mathsf{L} - \alpha\mathsf{M})\frac{\partial \hat{\boldsymbol{q}}}{\partial \omega}, \hat{\boldsymbol{q}}^\dagger \rangle = \langle \frac{\partial \alpha}{\partial \omega}\mathsf{M}\hat{\boldsymbol{q}}, \hat{\boldsymbol{q}}^\dagger \rangle. \tag{2.7}$$

Substitution of Eq. (2.4) for the second term on the left-hand side yields

$$\langle \frac{\partial \mathsf{L}}{\partial \omega}\hat{\boldsymbol{q}}, \hat{\boldsymbol{q}}^\dagger \rangle = \frac{\partial \alpha}{\partial \omega}\langle \mathsf{M}\hat{\boldsymbol{q}}, \hat{\boldsymbol{q}}^\dagger \rangle. \tag{2.8}$$

Solving for the group velocity, we thus obtain

$$c_g = \left(\frac{\langle \frac{\partial \mathsf{L}}{\partial \omega}\hat{\boldsymbol{q}}, \hat{\boldsymbol{q}}^\dagger \rangle}{\langle \mathsf{M}\hat{\boldsymbol{q}}, \hat{\boldsymbol{q}}^\dagger \rangle} \right)^{-1}. \tag{2.9}$$

The adjoint eigenvalue problem therefore allows the immediate and accurate evaluation of the group velocity of all eigensolutions, and as such their classification into downstream- and upstream-traveling solutions. Once this information has been obtained, we project the solution of the marching procedure onto the subspace spanned by the downstream-traveling modes, thus eliminating the contributions by the upstream-traveling solutions for which the spatial marching scheme describes an ill-posed procedure. Computation of the full spectrum of the inflated eigenvalue problem, Eq. (2.3), yields an $8n \times 8n$ matrix whose columns represent the eigenfunctions of the inflated state and n represents the number of discretized points in the wall-normal direction. We are interested in constructing an appropriate basis for the primitive variables of size $4n \times 4n$. The elimination of unphysical solutions attributed to the inflation of the system, as well as of unwanted upstream-traveling modes with $c_g < 0$, reduces the number of the remaining eigenfunctions to $k \leq 4n$ for the cases studied here. We arrange the first four rows representing the primitive variables, $[\hat{u}, \hat{v}, \hat{w}, \hat{p}]^{\mathsf{T}}$, of the retained eigenfunctions as the columns of the $4n \times k$ operator E_0. As such, this matrix contains the primitive variables of the relevant downstream-traveling modes.

To obtain a full basis of size $4n$, we fill further $4n-k$ columns with complex random vectors, $\boldsymbol{a}_i$, leading to a square matrix of size $4n \times 4n$

$$\mathsf{E}_1 = \begin{bmatrix} | & | & | & & | \\ \mathsf{E}_0 & \boldsymbol{a}_{k+1} & \boldsymbol{a}_{k+2} & \dots & \boldsymbol{a}_{4n} \\ | & | & | & & | \end{bmatrix}. \tag{2.10}$$

Performing a QR decomposition of E_1 without pivoting produces the orthogonal matrix E of size $4n \times 4n$

$$\mathsf{E} = \begin{bmatrix} | & | & | & & | \\ \mathsf{E}_\perp^\oplus & \boldsymbol{b}_{k+1} & \boldsymbol{b}_{k+2} & \dots & \boldsymbol{b}_{4n} \\ | & | & | & & | \end{bmatrix}, \tag{2.11a}$$

$$\mathsf{E} = \begin{bmatrix} \mathsf{E}_\perp^\oplus & \mathsf{B} \end{bmatrix}, \tag{2.11b}$$

where $\mathsf{E}_\perp^\oplus$ contains the orthogonal basis of the k physical and downstream-traveling modes and B contains the remainder of the orthogonal basis, which can be thought to represent unphysical or upstream-traveling solutions. Since E has full rank, any arbitrary solution vector, $\hat{\boldsymbol{q}}$, can be represented as a weighted superposition of the columns of E,

$$\hat{\boldsymbol{q}} = \mathsf{E}\boldsymbol{c}, \tag{2.12}$$

where $\boldsymbol{c}$ is a column vector whose j-th entry represents the weight of the j-th column of E in the construction of $\hat{\boldsymbol{q}}$. Because E is orthogonal, we can identify the weights by multiplying $\mathsf{E}^\mathsf{H} \equiv \mathsf{E}^{-1}$.

The following reconstruction of the solution $\hat{\boldsymbol{q}}$ in terms of downstream-traveling modes is based on the operator $\mathsf{E}^\oplus$, whose kernel covers rows of $\boldsymbol{c}$ representing the unwanted solutions,

$$\mathsf{E}^\oplus = \begin{bmatrix} | & | & & | \\ \mathsf{E}_\perp^\oplus & 0 & \dots & 0 \\ | & | & & | \end{bmatrix}. \tag{2.13}$$

With these operators, we can express the filtering of the arbitrary solution $\hat{\boldsymbol{q}}$ to retain only downstream-traveling solutions as

$$\hat{\boldsymbol{q}}^\oplus = \mathsf{E}^\oplus \mathsf{E}^H \hat{\boldsymbol{q}}. \tag{2.14}$$

2.2. *Results*

We will now demonstrate the above-presented filtering technique as applied in the streamwise marching of two eigenfunctions. We consider parallel boundary layer flow with Reynolds number based on the displacement thickness of $Re_\delta = 1000$. The non-dimensional frequency of the considered perturbations is $F = 10^6\omega/Re = 260$. The complex streamwise wavenumbers of the eigensolutions are $\alpha_1 = 0.54 + 0.08i$ and $\alpha_2 = 0.74 + 0.35i$. The current marching scheme resolves all the gradients in the streamwise coordinate on the grid. Roughly 100 points are used per streamwise length scale for the rapidly decaying mode, $h_x = 1/(100\Im(\alpha_2))$.

We compare the result obtained with the marching scheme to the classical linear PSE (Figure 1). The continuous reconstruction of the solution in terms of downstream-traveling eigenfunctions based on the group velocity leads to a stable marching procedure which allows the accurate computation of the evolution of perturbations for arbitrary grid spacings. In contrast, the solution obtained from the classical PSE rapidly diverges.

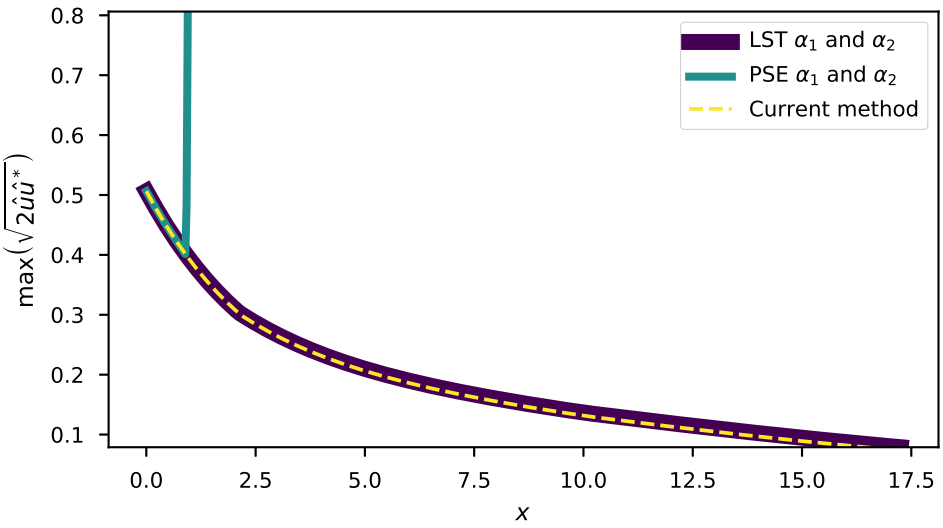

FIGURE 1. Amplitude of u'_{rms} versus streamwise location for filtering technique applied to the linear PSE by marching two stable modes and resolving the streamwise variation in the state vector in a parallel boundary layer. No filtering leads to the expected overflow. Filtering after each step leads to a stable marching procedure.

3. Capturing high-amplitude perturbations

We now turn our focus to deriving a spatial marching technique suitable for high-amplitude perturbations. The approach computes the mean-flow distortion owing to the nonlinear interactions of perturbations as part of the base flow as opposed to treating it like other perturbation harmonics. We note that this development is separate from the previous section. The implementation shown in the following still contains the typical ill-conditioned spatial marching of the PSE.

3.1. *Governing equations in incompressible flows*

In the following, we present the treatment of the base flow in our method, followed by the perturbation equations.

3.1.1. *Base flow*

The classical PSE commonly use similarity solutions such as the Blasius boundary layer solution to obtain a base flow which is then prescribed in the marching of the perturbations. In this setting, the mean-flow distortion is treated like other perturbation harmonics, although a different set of boundary conditions is prescribed (see, e.g., Lozano-Durán *et al.* 2018). The current approach obtains the base flow from a marching procedure operating on the modified boundary layer equations. In this setting, the MFD is computed as part of the base flow via the introduction of forcing terms which represent the perturbations.

The derivation of the marching procedure for the base flow starts from the Navier-Stokes equations. We decompose the state vector into a base state, denoted by an overbar, and a perturbation component, denoted by a prime: $\mathbf{q} = [u, v, w, p]^{\mathsf{T}} = \overline{\mathbf{q}}+\mathbf{q}'$. Introduction

of this decomposition into the governing equations gives

$$\frac{\partial(\overline{u}+u')_i}{\partial t}+(\overline{u}+u')_j\frac{\partial(\overline{u}+u')_i}{\partial x_j}+\frac{\partial(\overline{p}+p')}{\partial x_i}-\frac{1}{Re}\frac{\partial^2(\overline{u}+u')_i}{\partial x_j\partial x_j}=0. \tag{3.1}$$

Here, we have made use of Einstein's index notation for the Cartesian coordinates and Re, p, and u indicate the Reynolds number, pressure, and velocity, respectively. We note that the above decomposition differs from that applied in the PSE, where the average of the perturbation component represents the MFD, implying that $\overline{\boldsymbol{q'}}\neq 0$. In the present case, the mean-flow distortion is absorbed into the base state so that the average of the fluctuation component vanishes.

Taking the average of Eq. (3.1), we thus obtain

$$\frac{\partial\overline{u}_i}{\partial t}+\overline{u}_j\frac{\partial\overline{u}_i}{\partial x_j}+\overline{u'_j\frac{\partial u'_i}{\partial x_j}}+\frac{\partial\overline{p}}{\partial x_i}-\frac{1}{Re}\frac{\partial^2\overline{u}_i}{\partial x_j\partial x_j}=0. \tag{3.2}$$

Under the assumption of steady, two-dimensional, and incompressible flow, the above equations are reduced to the x and y momentum equations,

$$\overline{u}\frac{\partial\overline{u}}{\partial x}+\overline{v}\frac{\partial\overline{u}}{\partial y}+\overline{u'_j\frac{\partial u'}{\partial x_j}}+\frac{\partial\overline{p}}{\partial x}-\frac{1}{Re}\left(\frac{\partial^2\overline{u}}{\partial x^2}+\frac{\partial^2\overline{u}}{\partial y^2}\right)=0, \tag{3.3a}$$

$$\overline{u}\frac{\partial\overline{v}}{\partial x}+\overline{v}\frac{\partial\overline{v}}{\partial y}+\overline{u'_j\frac{\partial v'}{\partial x_j}}+\frac{\partial\overline{p}}{\partial y}-\frac{1}{Re}\left(\frac{\partial^2\overline{v}}{\partial x^2}+\frac{\partial^2\overline{v}}{\partial y^2}\right)=0. \tag{3.3b}$$

Following the derivation of the classical boundary layer equations (White 1974), we introduce the non-dimensional scaling for velocity, pressure, and spatial location

$$x=\frac{x^*}{L^*},y=\frac{y^*}{L^*}\sqrt{Re},\overline{u}=\frac{\overline{u}^*}{u^*_\infty},\overline{v}=\frac{\overline{v}^*}{u^*_\infty}\sqrt{Re},\text{ and }\overline{p}=\frac{\overline{p}^*-p^*_\infty}{\rho^*u^{*2}_\infty}. \tag{3.4}$$

In Eq. (3.4) the reference values u^*_∞ is the constant free-stream velocity, L^* is the length scale of the problem, p^*_∞ is the reference pressure, and the star (*) indicates dimensional quantities. Considering the limit $Re=\rho^*u^*_\infty L^*/\mu^*\rightarrow\infty$, we arrive at the modified boundary layer equations,

$$\frac{\partial\overline{u}}{\partial x}+\frac{\partial\overline{v}}{\partial y}=0, \tag{3.5a}$$

$$\overline{u}\frac{\partial\overline{u}}{\partial x}+\overline{v}\frac{\partial\overline{u}}{\partial y}+\frac{\partial\overline{p}}{\partial x}-\frac{1}{Re}\left(\frac{\partial^2\overline{u}}{\partial y^2}\right)=-\overline{u'_j\frac{\partial u'}{\partial x_j}}, \tag{3.5b}$$

$$\frac{\partial\overline{p}}{\partial y}=-\overline{u'_j\frac{\partial v'}{\partial x_j}}. \tag{3.5c}$$

The averaged perturbation terms on the right-hand side act as forcing terms and are computed in the perturbation equations. Splitting the equations into operator form and applying an implicit Euler integration method in the streamwise coordinate, we arrive at a system of equations

$$\mathcal{A}_{i+1}\bar{\mathbf{q}}_{i+1}=\mathbf{b}_i. \tag{3.6}$$

These equations can be solved in an iterative fashion coupled with the perturbation equations to yield a marching procedure for the base, flow as outlined below and shown in Figure 2. The operator definitions are provided in Eq. (B 1) in Appendix B.

3.1.2. *Perturbation equations*

The derivation of the equations governing the nonlinear evolution of perturbations takes the decomposed Navier-Stokes equations, Eq. (3.1), and subtracts the averaged momentum equations, Eq. (3.2), to obtain

$$\underbrace{\frac{\partial u_i'}{\partial t} + \bar{u}_j \frac{\partial u_i'}{\partial x_j} + u_j' \frac{\partial \bar{u}_i}{\partial x_j} + \frac{\partial p'}{\partial x_i} - \frac{1}{Re} \frac{\partial^2 u_i'}{\partial x_j \partial x_j} = -u_j' \frac{\partial u_i'}{\partial x_j}}_{\text{Classical PSE terms}} + \underbrace{\overline{u_j' \frac{\partial u_i'}{\partial x_j}}}_{\text{Additional terms}} \quad . \tag{3.7}$$

Comparing this equation with the classical PSE, the right-hand side contains an additional averaged nonlinear term which relates the base state to the perturbation equations. Consistent with the classical PSE, we assume our perturbation state to take the form

$$\mathbf{q}'(x, y, z, t) = \hat{\mathbf{q}}(x, y, z) e^{\left(\mathrm{i} \int_{x_0}^{x} \alpha(\xi) d\xi - \mathrm{i}\omega t\right)}. \tag{3.8}$$

Here, $\hat{\mathbf{q}} = [\hat{u}, \hat{v}, \hat{w}, \hat{p}]^T$ denotes slowly varying quantities in x, while the exponential factor represents the fast varying part of perturbation quantities. In the present application to high-amplitude, low-frequency streaks, both α and ω are taken to be effectively zero, and thus we are neglecting this part of the ansatz. In the following, we thus assume a steady-state solution for this application.

Introduction of this ansatz into Eq. (3.7) and retaining terms of $\mathcal{O}(1/Re)$, we obtain the perturbation equations

$$\mathcal{M}_{i+1} \hat{\mathbf{q}}_{i+1} = \boldsymbol{d}_i. \tag{3.9}$$

Here, the first term on the left-hand side of Eq. (3.7) is accounted for by the linear operator $\mathcal{M}_{i+1}$ and the averaged nonlinear terms are being treated as the forcing term $\boldsymbol{d}_i$. Definitions of $\mathcal{M}$ and $\boldsymbol{d}_i$ are given in Appendix C. Homogeneous boundary conditions,

$$\hat{u} = \hat{v} = \hat{w} = 0, \tag{3.10}$$

are imposed at the wall, $y = 0$, and in the free stream, $y = \infty$.

3.1.3. *Solution method*

A schematic of the numerical method used to solve the systems of equations in Eq. (3.6) and (3.9) is presented in Figure 2. An iterative procedure is implemented with the streamwise marching procedure to simultaneously advance the base flow and the perturbations.

3.2. *Results*

In the following, we apply our method in the computation of the evolution of high-amplitude perturbations in a boundary layer. The inlet profile of the perturbations is computed in optimal growth analysis (Hack & Moin 2017) and describes a row of counter-rotating vortices, as depicted in Figure 3. By means of the lift-up mechanism, the vortices vertically displace the momentum of the boundary layer and thus generate highly energetic perturbations in the streamwise velocity component.

The Reynolds number based on the Blasius length scale is $Re_{\delta_b} = 162.6$, and the spanwise wavenumber for the periodic vortices is $\beta = 0.377$. The maximum fluctuation amplitude at the inflow location is $\max(||\vec{u}||) = 0.0373$, which induced appreciable nonlinear effects. For the purpose of comparison, a direct numerical simulation (DNS) of the same conditions was also conducted. Results in terms of the Fourier transformed streamwise velocity component are presented in Figure 4. Excellent agreement with the DNS

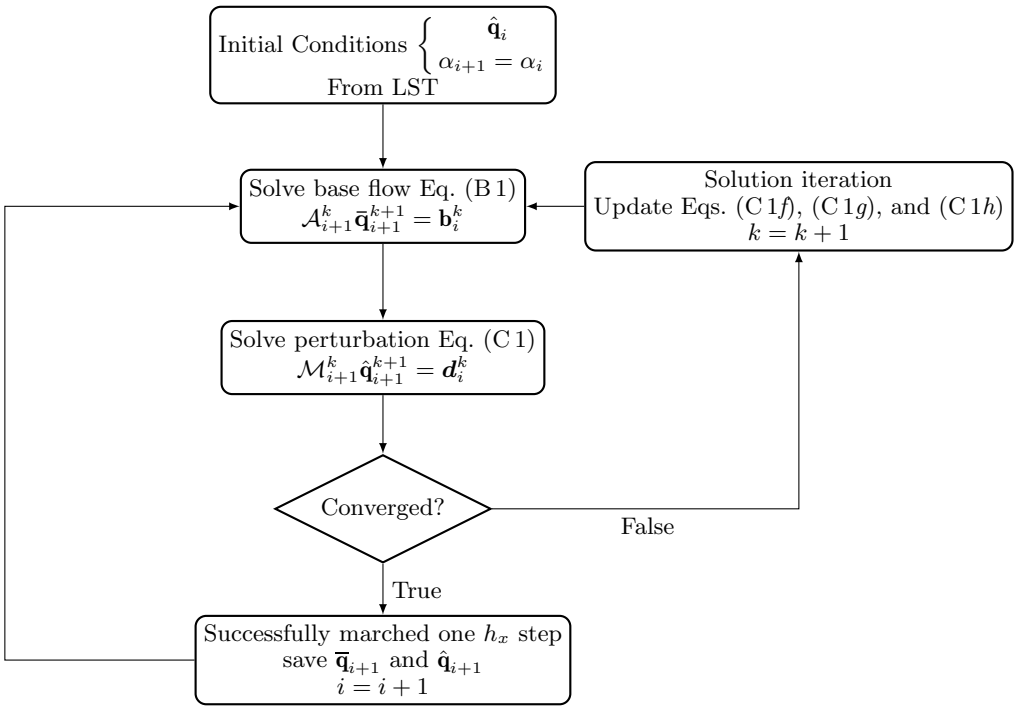

FIGURE 2. Solution procedure for the present method. The superscript k indicates the solution iteration, and the subscript i indicates the spatial streamwise marched step.

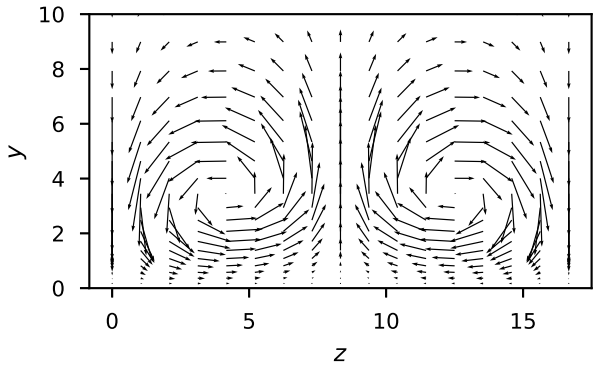

FIGURE 3. Spanwise cross-plane at the inlet ($x = 0$) of the flat plate case near the boundary layer. The arrows depict the plane velocity directions.

data is observed for all considered harmonics. The outcome indicates that the method presented herein can accurately capture the evolution of high-amplitude perturbations. Comparison between the streamwise velocity fluctuations at $x = 951.3$ in Figure 5 fur-

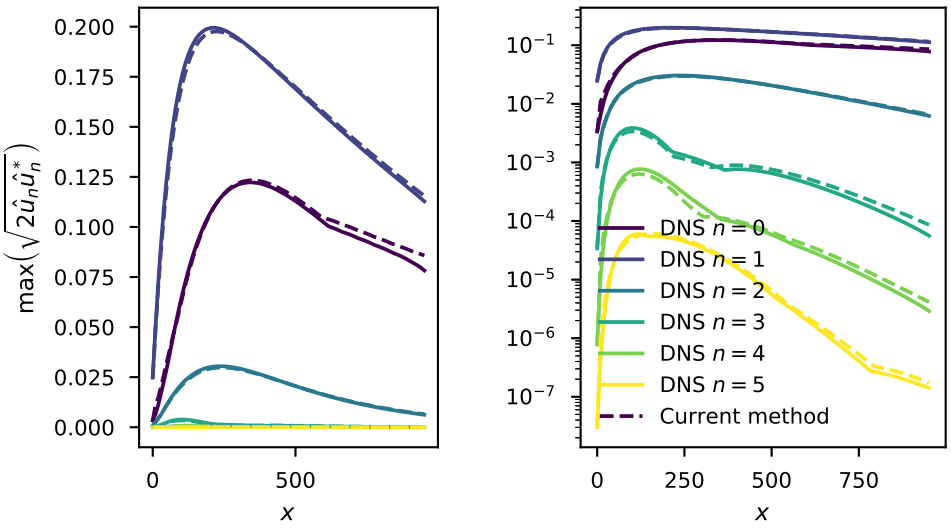

(a) (b)

FIGURE 4. Comparison of the amplitude of u'_{rms} for the spanwise modes of the streamwise Fourier transformed velocity perturbations ($\hat{u}_n$) about the Blasius boundary layer profile. The velocity perturbations calculated from DNS ($u_{\text{DNS}} - u_{\text{blas}}$) and the current method ($\overline{u} + u' - u_{\text{blas}}$) for the first 5 modes ($n = 1$ to 5) and the MFD ($n = 0$) are shown on (a) linear and (b) log scale.

ther substantiates the capability of the present method to accurately capture the highly energetic streaks.

4. Conclusions

The PSE have been widely applied in the computation of perturbations in boundary layer flows. The formulation of the PSE nonetheless has several limitations which, depending on the setting, may undermine the stability and accuracy of the approach. In this work, we have presented a solution procedure which overcomes the two key shortcomings of the PSE.

As has been widely recognized in the literature, the PSE formulation is in fact not fully parabolic, which can result in numerical divergence. In this work, we have shown that a decomposition of the state into upstream- and downstream-traveling solutions, identified by the group velocity of the corresponding eigensolutions, can resolve this key limitation. The projection of the state onto the subspace spanned by downstream-traveling solutions stabilizes the marching scheme for arbitrary streamwise step size, and without modification of the governing equations.

In addition, we have introduced a method for the accurate computation of high-amplitude perturbations within a spatial marching scheme. The PSE treat the mean-flow distortion introduced by harmonic interactions in a similar fashion to other harmonics, which can undermine the accuracy and numerical stability in settings with high perturbation amplitudes. Our approach evolves the mean-flow distortion as part of the base

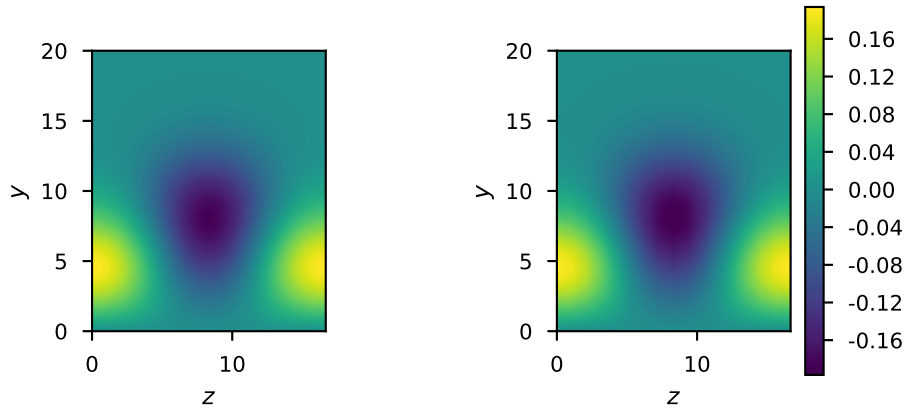

(a) (b)

FIGURE 5. The contours of the fluctuations in the streamwise direction relative to the Blasius boundary layer profile at the same streamwise location, $x = 951.3$, obtained from (a) DNS and (b) the current model.

flow in a coupled spatial marching scheme. Comparison with DNS demonstrated excellent agreement for high-amplitude perturbations.

Appendix A. Linear stability theory (LST) operators

The operators for the LST are shown here. Assuming we have a locally parallel flow, we can define the spatial eigenvalue problem of the second-order polynomial eigenvalue as a first-order eigenvalue problem as

$$\mathsf{L}\hat{\boldsymbol{q}} = \alpha \mathsf{M}\hat{\boldsymbol{q}}, \tag{A 1a}$$

$$\mathsf{L} = \begin{bmatrix} 0 & 0 & 0 & 0 & 1 & 0 & 0 & 0 \\ 0 & 0 & 0 & 0 & 0 & 1 & 0 & 0 \\ 0 & 0 & 0 & 0 & 0 & 0 & 1 & 0 \\ 0 & 0 & 0 & 0 & 0 & 0 & 0 & 1 \\ \Delta & -ReU_y & 0 & 0 & -iReU & 0 & 0 & -iRe \\ 0 & \Delta & 0 & -ReD_y & 0 & -iReU & 0 & 0 \\ 0 & 0 & \Delta & -iRe\beta & 0 & 0 & -iReU & 0 \\ 0 & D_y & i\beta & 0 & i & 0 & 0 & 0 \end{bmatrix}, \tag{A 1b}$$

$$\hat{\boldsymbol{q}} = \left[\hat{u}, \hat{v}, \hat{w}, \hat{P}, \alpha\hat{u}, \alpha\hat{v}, \alpha\hat{w}, \alpha\hat{P}\right]^{\mathsf{T}}, \tag{A 1c}$$

$$\mathsf{M} = \begin{bmatrix} 1 & 0 & 0 & 0 & 0 & 0 & 0 & 0 \\ 0 & 1 & 0 & 0 & 0 & 0 & 0 & 0 \\ 0 & 0 & 1 & 0 & 0 & 0 & 0 & 0 \\ 0 & 0 & 0 & 1 & 0 & 0 & 0 & 0 \\ 0 & 0 & 0 & 0 & 1 & 0 & 0 & 0 \\ 0 & 0 & 0 & 0 & 0 & 1 & 0 & 0 \\ 0 & 0 & 0 & 0 & 0 & 0 & 1 & 0 \\ 0 & 0 & 0 & 0 & 0 & 0 & 0 & 0 \end{bmatrix}, \tag{A 1d}$$

$$\Delta = iRe\omega + (D_{yy} - \beta^2). \tag{A 1e}$$

Appendix B. Boundary layer operators

The operators for the boundary layer base flow is presented here. Splitting the modified boundary layer equations shown in Eq. (3.5) into operator form, we obtain

$$[\mathbf{A} + (\mathbf{B} + \mathbf{B}_F)\mathcal{D}_y + \mathbf{C}\mathcal{D}_{yy} + (\mathbf{D} + \mathbf{D}_F)\mathcal{D}_x]\bar{\mathbf{q}} = -\overline{\mathbf{F}}, \tag{B 1a}$$

with the operators

$$\mathbf{A} = \begin{bmatrix} 0 & 0 & 0 \\ 0 & 0 & 0 \\ 0 & 0 & 0 \end{bmatrix}, \quad \mathbf{B} = \begin{bmatrix} 0 & 0 & 0 \\ 0 & 0 & 1 \\ 0 & 1 & 0 \end{bmatrix}, \quad \mathbf{B}_F = \begin{bmatrix} \overline{v}^k & 0 & 0 \\ 0 & 0 & 0 \\ 0 & 0 & 0 \end{bmatrix},$$

$$\mathbf{C} = \begin{bmatrix} -\frac{1}{Re} & 0 & 0 \\ 0 & 0 & 0 \\ 0 & 0 & 0 \end{bmatrix}, \quad \mathbf{D} = \begin{bmatrix} 0 & 0 & 1 \\ 0 & 0 & 0 \\ 1 & 0 & 0 \end{bmatrix}, \quad \mathbf{D}_F = \begin{bmatrix} \overline{u}^k & 0 & 0 \\ 0 & 0 & 0 \\ 0 & 0 & 0 \end{bmatrix}, \tag{B 1b}$$

$$\overline{\mathbf{F}} = \begin{bmatrix} \overline{u'\frac{\partial u'}{\partial x}} + \overline{v'\frac{\partial u'}{\partial y}} + \overline{w'\frac{\partial u'}{\partial z}} \\ \overline{u'\frac{\partial v'}{\partial x}} + \overline{v'\frac{\partial v'}{\partial y}} + \overline{w'\frac{\partial v'}{\partial z}} \\ 0 \end{bmatrix}.$$

Here, $\bar{\mathbf{q}}$ is the base flow state vector $\bar{\mathbf{q}}(x, y) = [\overline{u}, \overline{v}, \overline{p}]^T$, $\mathcal{D}_y$ indicates the first derivative in the y direction, and $\mathcal{D}_{yy}$ indicates the second derivative with respect to the y axis. In the present study, these derivative operators were implemented using fourth-order finite differences, and similar operators are used in the perturbation equations. The streamwise derivative operator is integrated using the implicit Euler integration.

Introducing the implicit Euler method and integrating, we arrive at an equation of the form

$$\mathcal{A}_{i+1}\bar{\mathbf{q}}_{i+1} = \mathbf{b}_i, \tag{B 1c}$$

or alternatively,

$$\left[\mathbf{A} + (\mathbf{B} + \mathbf{B}_F)\mathcal{D}_y + \mathbf{C}\mathcal{D}_{yy} + \frac{\mathbf{D} + \mathbf{D}_F}{h_x}\right]_{i+1} \bar{\mathbf{q}}_{i+1} = \frac{(\mathbf{D} + \mathbf{D}_F)_{i+1}}{h_x}\bar{\mathbf{q}}_i - \overline{\mathbf{F}}_{i+1}. \tag{B 1d}$$

Here, $\mathcal{A}$ and $\mathbf{b}_i$ can be defined by comparing the two above equations. This equation can be solved for each streamwise step, where the operators are defined in Eq. (B 1*b*). This base flow is updated at each iterative step, as depicted in Figure 2. Note that the boundary conditions will contain the no-slip condition at the wall, the free-stream velocity u_∞ at the free stream and an initial known inlet condition. The current study used the Blasius boundary layer solution as the inlet for the preliminary results.

Appendix C. Perturbation equation operators

The operators for the perturbation equation are described in detail here. Note that the $\mathcal{D}_x$ operator uses the implicit Euler method to march downstream in the slowly varying flow. The subscript F on the operators indicates the non-averaged, nonlinear terms that have been linearized by lagging a state vector in a nonlinear iterative loop as is described by DeBlois (1997). It should be noted that the averaged nonlinear terms could also have this lagging; however, it may disrupt much of the sparse nature of finite difference operator form and was not pursued in this work. Introducing the operator form, the perturbation equations are written as

$$[\mathbf{A}+\mathbf{A}_F+(\mathbf{B}+\mathbf{B}_F)\mathcal{D}_y+(\mathbf{C}+\mathbf{C}_F)\mathcal{D}_{yy}+(\mathbf{D}+\mathbf{D}_F)\mathcal{D}_x+(\mathbf{E}+\mathbf{E}_F)\mathcal{D}_z+(\mathbf{G}+\mathbf{G}_F)\mathcal{D}_{zz}]\hat{\mathbf{q}}=\overline{\mathbf{F}}_p. \tag{C 1a}$$

Introducing the implicit Euler for the $\mathcal{D}_x$ will give us the governing system of equations as shown in Eq. (C 1*b*) with operator and right-hand side defined in Eqs. (C 1*c*), (C 1*e*), (C 1*f*), and (C 1*g*). The subscripts i and $i+1$ denote the spatial marching step of step size h_x, where i is the current spatial step, and $i+1$ is the unknown next marching step.

$$\mathcal{M}_{i+1}\hat{\mathbf{q}}_{i+1}=\boldsymbol{d}_i, \tag{C 1b}$$

$$\boldsymbol{d}_i=(\overline{\mathbf{F}}_p)_{i+1}+\frac{\mathbf{D}_{i+1}+(\mathbf{D}_F)_{i+1}}{h_x}\hat{\mathbf{q}}_i, \tag{C 1c}$$

$$\mathcal{M}=\mathbf{A}+\mathbf{A}_F+(\mathbf{B}+\mathbf{B}_F)\mathcal{D}_y+(\mathbf{C}+\mathbf{C}_F)(\mathcal{D}_{yy}+\mathcal{D}_{zz})+\frac{\mathbf{D}+\mathbf{D}_F}{h_x}+(\mathbf{E}+\mathbf{E}_F)\mathcal{D}_z, \tag{C 1d}$$

$$\begin{aligned}
\mathbf{A}&=\begin{bmatrix} r+\bar{u}_x & \bar{u}_y & 0 & i\alpha \\ 0 & r+\bar{v}_y & 0 & 0 \\ 0 & 0 & r & 0 \\ i\alpha & 0 & 0 & 0 \end{bmatrix}, \quad \mathbf{B}=\begin{bmatrix} \bar{v} & 0 & 0 & 0 \\ 0 & \bar{v} & 0 & 1 \\ 0 & 0 & \bar{v} & 0 \\ 0 & 1 & 0 & 0 \end{bmatrix}, \\
\mathbf{C}&=\begin{bmatrix} \frac{-1}{Re} & 0 & 0 & 0 \\ 0 & \frac{-1}{Re} & 0 & 0 \\ 0 & 0 & \frac{-1}{Re} & 0 \\ 0 & 0 & 0 & 0 \end{bmatrix}, \qquad \mathbf{D}=\begin{bmatrix} \bar{u} & 0 & 0 & 1 \\ 0 & \bar{u} & 0 & 0 \\ 0 & 0 & \bar{u} & 0 \\ 1 & 0 & 0 & 0 \end{bmatrix}, \\
\mathbf{E}&=\begin{bmatrix} 0 & 0 & 0 & 0 \\ 0 & 0 & 0 & 0 \\ 0 & 0 & 0 & 1 \\ 0 & 0 & 1 & 0 \end{bmatrix}, \\
r&=-i\omega+i\alpha\bar{u}+\frac{\alpha^2}{Re},
\end{aligned} \tag{C 1e}$$

$$\mathbf{A}_F = \begin{bmatrix} a_f & 0 & 0 & 0 \\ 0 & a_f & 0 & 0 \\ 0 & 0 & a_f & 0 \\ 0 & 0 & 0 & 0 \end{bmatrix}, \quad \mathbf{B}_F = \begin{bmatrix} b_f & 0 & 0 & 0 \\ 0 & b_f & 0 & 0 \\ 0 & 0 & b_f & 0 \\ 0 & 0 & 0 & 0 \end{bmatrix},$$
$$\mathbf{C}_F = \begin{bmatrix} 0 & 0 & 0 & 0 \\ 0 & 0 & 0 & 0 \\ 0 & 0 & 0 & 0 \\ 0 & 0 & 0 & 0 \end{bmatrix}, \qquad \mathbf{D}_F = \begin{bmatrix} d_f & 0 & 0 & 0 \\ 0 & d_f & 0 & 0 \\ 0 & 0 & d_f & 0 \\ 0 & 0 & 0 & 0 \end{bmatrix}, \tag{C 1f}$$
$$\mathbf{E}_F = \begin{bmatrix} e_f & 0 & 0 & 0 \\ 0 & e_f & 0 & 0 \\ 0 & 0 & e_f & 0 \\ 0 & 0 & 0 & 0 \end{bmatrix}.$$

Here, Eq. (C 1*g*) defines the individual components of the nonlinear operators. The superscript k denotes the previous iteration's guess for the current quantities. The nonlinear coefficients are defined as

$$\begin{aligned} a_f &= \hat{u}^k \mathrm{i}\alpha e^{\mathrm{i}\Theta}, \qquad & b_f &= \hat{v}^k e^{\mathrm{i}\Theta}, \\ d_f &= \hat{u}^k e^{\mathrm{i}\Theta}, \qquad & e_f &= \hat{w}^k e^{\mathrm{i}\Theta}, \\ \Theta &= \int_{x_0}^{x} \alpha(\xi) d\xi. \end{aligned} \tag{C 1g}$$

The averaged forcing nonlinear terms are defined as

$$\overline{\mathbf{F}}_p = \begin{bmatrix} \overline{u' \frac{\partial u'}{\partial x}} + \overline{v' \frac{\partial u'}{\partial y}} + \overline{w' \frac{\partial u'}{\partial z}} \\ \overline{u' \frac{\partial v'}{\partial x}} + \overline{v' \frac{\partial v'}{\partial y}} + \overline{w' \frac{\partial v'}{\partial z}} \\ \overline{u' \frac{\partial w'}{\partial x}} + \overline{v' \frac{\partial w'}{\partial y}} + \overline{w' \frac{\partial w'}{\partial z}} \\ 0 \end{bmatrix}. \tag{C 1h}$$

This term is the new additional term introduced by the current model when compared to the classical PSE derivation.

Acknowledgments

This investigation was funded by Sandia National Laboratories and conducted at Stanford University. The authors acknowledge use of computational resources from the Certainty cluster awarded by the National Science Foundation to CTR.

REFERENCES

Andersson, P., Henningson, D. S. & Hanifi, A. 1998 On a stabilization procedure for the parabolic stability equations. *J. Eng. Math.* **33**, 311–332.

Chang, C. L., Malik, M. R., Erlebacher, G. & Hussaini, M. Y. 1991 Compressible stability of growing boundary layers using parabolized stability equations. *AIAA Paper* 1991-7262.

DeBlois, B. M. 1997 Linearizing convection terms in the Navier-Stokes equations. *Comput. Method Appl. M.* **143**, 289–297.

Hack, M. J. P. & Moin, P. 2017 Algebraic disturbance growth by interaction of Orr and lift-up mechanisms. *J. Fluid Mech.* **829**, 112–126.

Haj-Hariri, H. 1994 Characteristics analysis of the parabolized stability equations. *Stud. Appl. Math.* **92**, 41–53.

Herbert, T. 1997 Parabolized stability equations. *Annu. Rev. Fluid Mech.* **29**, 245–283.

Li, F. & Malik, M. R. 1996 On the nature of PSE approximation. *Theor. Comp. Fluid Dyn.* **8**, 253–273.

Li, F. & Malik, M. R. 1997 Spectral analysis of parabolized stability equations. *Comput. Fluids* **26**, 279–297.

Lozano-Durán, A., Hack, M. J. P. & Moin, P. 2018 Modeling boundary-layer transition in direct and large-eddy simulations using parabolized stability equations. *Phys. Rev. Fluids* **3**, 023901.

Ran, W., Zare, A., Hack, M. J. P. & Jovanović, M. R. 2019 Modeling mode interactions in boundary layer flows via the Parabolized Floquet Equations. *Phys. Rev. Fluids* **4**, 023901.

Towne, A. & Colonius, T. 2015 One-way spatial integration of hyperbolic equations. *J. Comput. Phys.* **300**, 844–861.

Towne, A., Rigas, G. & Colonius, T. 2019 A critical assessment of the parabolized stability equations. *Theor. Comp. Fluid Dyn.* **33**, 359–382.

White, F. M. 1974 *Viscous Fluid Flow*. McGraw-Hill New York.